



RESEARCH ARTICLE | JUNE 12 2023

Direct numerical simulations of polypropylene gasification in supercritical water

Chi Cheng (池成) ; Guan Wei (管伟); Ou Zhisong (欧治松); Kai Sundmacher; Dominique Thévenin 

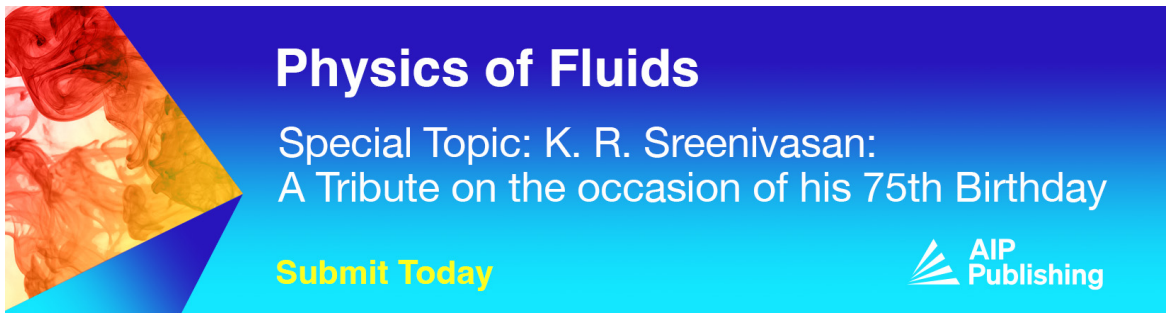


Physics of Fluids 35, 063321 (2023)

<https://doi.org/10.1063/5.0155831>




CrossMark



Physics of Fluids
Special Topic: K. R. Sreenivasan:
A Tribute on the occasion of his 75th Birthday

Submit Today



Direct numerical simulations of polypropylene gasification in supercritical water

Cite as: Phys. Fluids **35**, 063321 (2023); doi: [10.1063/5.0155831](https://doi.org/10.1063/5.0155831)

Submitted: 24 April 2023 · Accepted: 29 May 2023 ·

Published Online: 12 June 2023





View Online



Export Citation



CrossMark

Cheng Chi (池成),^{1,a)}  Wei Guan (管伟),^{1,2} Zhisong Ou (欧治松),^{3,4} Kai Sundmacher,^{5,6} and Dominique Thévenin¹ 

AFFILIATIONS

¹Laboratory of Fluid Dynamics and Technical Flows, University of Magdeburg "Otto von Guericke", D-39106 Magdeburg, Germany

²Institute for Energy Research, Jiangsu University, Zhenjiang 212013, China

³State Key Laboratory of Geomechanics and Geotechnical Engineering, Institute of Rock and Soil Mechanics, Chinese Academy of Sciences, Wuhan 430071, China

⁴State Key Laboratory of Multiphase Flow in Power Engineering, Xi'an Jiaotong University, Xi'an 710049, China

⁵Laboratory of Process Systems Engineering, University of Magdeburg "Otto von Guericke", D-39106 Magdeburg, Germany

⁶Process Systems Engineering, Max Planck Institute for Dynamics of Complex Technical Systems, D-39106 Magdeburg, Germany

^{a)} Author to whom correspondence should be addressed: cheng.chi@ovgu.de

ABSTRACT

In order to reduce environmental pollution by plastic wastes, supercritical water gasification (SCWG) appears as a promising technology. The present study investigates the SCWG process of polypropylene (PP) plastic waste using particle-resolved direct numerical simulations (PR-DNS). A directional ghost-cell immersed boundary method has been used to solve the reacting boundary condition, including detailed molecular diffusion models. To validate the procedure, SCWG of a coal particle has been first investigated as a benchmark, analyzing in detail interphase momentum and heat and mass transfer, and chemical reactions are analyzed. Surface reactions and the resulting Stefan flow expand the boundary layer around the particle, impacting the efficiency of heat and mass transfer. Adding then a suitable reaction mechanism, SCWG of PP plastic wastes leading to combustible gases is analyzed by PR-DNS and found to be very efficient. The gasification temperature is an important parameter to control SCWG efficiency. To the authors' knowledge, this is the first PR-DNS study investigating the SCWG process for plastic wastes, and it provides interesting information regarding transfer processes and their limitations.

© 2023 Author(s). All article content, except where otherwise noted, is licensed under a Creative Commons Attribution (CC BY) license (<http://creativecommons.org/licenses/by/4.0/>). <https://doi.org/10.1063/5.0155831>

I. INTRODUCTION

With the rapidly growing usage of plastic products in our daily life, the management of waste plastics is becoming more and more important for the environment. Due to the degradation resistance of plastics, a direct abandon of them in the natural environment is extremely harmful.¹ Therefore, a smart and efficient way to recycle those waste plastics is in high demand.

Supercritical water gasification (SCWG) appears as one promising technique to recycle the waste plastics and convert them into combustible gases.^{2–7} SCWG was first used to convert coal/biomass into combustible gases with high content of H₂ and CO₂.^{8–12} The resulting CO₂ can be further converted into hydrocarbon fuel using renewable energy in the process.^{8,13} In that case, the whole process leads to zero CO₂ emission.

SCWG is usually operated at 400–650 °C and 250–350 bar.¹⁴ The thermochemical process involves surface reactions and interface heat

and mass transfer. A comprehensive understanding of this process is crucial for a practical application of SCWG in large-scale systems. Though experimental measurements could shed some light on this transient process, detailed investigations are impossible due to the very high operation pressure and high temperature. It is currently impossible to measure under operation details regarding flow field, surface reactions, and conversion of solid particles. As a complementary source of information, detailed numerical simulations could fully reveal every details of this complex process, provided suitable models are available. Among all numerical techniques, particle-resolved direct numerical simulation (PR-DNS) is emerging as the most accurate approach to investigate in detail particle/fluid interaction processes¹⁵—but leads, of course, to very high numerical costs.

PR-DNS with SCWG has been intensively developed in the last few years. Supercritical water flow around an inert particle was first investigated, studying the convective heat transfer characteristics.¹⁶

Later, the effect of inert particle sphericity on drag force and heat transfer in supercritical water was considered.¹⁷ In a further step, the effect of Stefan flow on drag force and heat transfer around an inert particle was considered and investigated for an incompressible flow¹⁸ or a variable-density flow.¹⁹ All these studies were considering inert particles, without surface reactions, therefore neglecting the Stefan flow taking place under real conditions. This aspect was the focus of our previous studies,^{20,21} taking into account more realistic conditions induced by the reactions, noticeably impacting all transfer processes around the particle.

In realistic applications, the temperature and species fields near the particle change due to the surface reactions, resulting in considerable modifications of the corresponding fluid properties. Recent works^{22–24} have demonstrated the influence of temperature-induced fluid property variation. In particular, the properties of SCW are found to be very sensitive to temperature. The influence of variable physical properties under supercritical condition for a flow over a spherical particle has been investigated in detail in Ref. 25. In addition, the Stefan flow due to the generation of gases at the reacting particle surface would impact the surrounding flow field.^{18,26,27} In reality, Stefan velocities are not uniformly distributed around the particle; assuming a uniform Stefan flow around the particle would not be realistic.¹⁷ For all these reasons, it appears necessary to consider with more accurate models a reacting particle using PR-DNS for a study of the SCWG process.

While supercritical water gasification of coal has been investigated in many numerical studies during the last few years,^{20,21,28–30} SCWG of waste plastics has, to the best of the authors' knowledge, never been investigated numerically. However, it shows a significant potential regarding both natural environment protection and clean energy production. Therefore, understanding the detailed hydrothermal process of SCWG for waste plastics is very important. The present study tries to fill the gap, thanks for a detailed investigation on SCWG for polypropylene (PP) particles using PR-DNS. Among all waste plastic components, polypropylene constitutes the largest amount³¹ and is, thus, considered in the present work. As far as we know, this is the first-ever PR-DNS study regarding SCWG of waste plastics. In what follows, Sec. II will introduce the numerical methods used for PR-DNS, the chemical kinetics, and the numerical configuration considered in the present study. The simulation results and the associated discussion are presented in Sec. III, discussing the interphase momentum, heat and mass transfer, and the impact of chemical reactions. Finally, conclusions are drawn in Sec. IV.

II. NUMERICAL METHODS

All employed numerical methods and models are introduced in this section. The SCWG process is considered in low-Mach number flows in the current study, which corresponds to the conditions found in reality regarding SCWG of coal.

A. Particle-resolved DNS

As in our previous studies for coal particle gasification,^{20,21} the DNS is carried out using our in-house low-Mach DNS solver DINO.^{32–35} The governing equations solved in DINO can be summarized as

$$\frac{\partial \rho}{\partial t} + \frac{\partial(\rho u_i)}{\partial x_j} = 0, \tag{1}$$

$$\frac{\partial(\rho u_i)}{\partial t} + \frac{\partial(\rho u_i u_j)}{\partial x_j} = -\frac{\partial p}{\partial x_i} + \frac{\partial}{\partial x_j} \left[\mu \left(\frac{\partial u_i}{\partial x_j} + \frac{\partial u_j}{\partial x_i} - \frac{2}{3} \frac{\partial u_k}{\partial x_k} \delta_{ij} \right) \right], \tag{2}$$

$$\frac{\partial T}{\partial t} + u_j \frac{\partial T}{\partial x_j} = -\frac{1}{\rho C_p} \left[\sum_{k=1}^{N_s} h_k \dot{\omega}_k - \frac{\partial}{\partial x_j} \left(\lambda \frac{\partial T}{\partial x_j} \right) + \frac{\partial T}{\partial x_j} \sum_{k=1}^{N_s} \rho C_{p,k} Y_k V_{k,j} \right], \tag{3}$$

$$\frac{\partial Y_k}{\partial t} + u_j \frac{\partial Y_k}{\partial x_j} = -\frac{\dot{\omega}_k}{\rho} - \frac{1}{\rho} \frac{\partial(\rho Y_k V_{k,j})}{\partial x_j}, \tag{4}$$

$$\rho = f(P_0, T, W, Y_k), \tag{5}$$

where ρ is the density, u_i is the velocity component in the i th direction, p is the fluctuation pressure, μ is the dynamic viscosity, δ_{ij} is the Kronecker delta, T is the temperature, C_p is the specific heat capacity at constant pressure, h_k is the specific enthalpy of species k , N_s is the total number of species, $\dot{\omega}_k$ is the mass production rate of species k , λ is the heat diffusion coefficient, Y_k is the mass fraction of species k , $V_{k,j}$ is the j th component of the molecular diffusion velocity for species k , P_0 is the thermodynamic pressure, and W is the mean molecular weight.

To solve the aforementioned equations, a sixth-order finite-difference scheme has been used for spatial discretization, while an explicit fourth-order Runge–Kutta scheme is implemented for temporal integration. The solver is pressure-based. The Poisson equation for pressure is implicitly solved with a fast spectral approach.³² The molecular diffusion in the gas phase is solved with a multi-component diffusion model based on the open-source library Cantera,³⁶ while the molecular diffusion for the surface gases is modeled using constant Lewis numbers (with values of Le set to 0.29 for H_2 , 1.09 for CO , 1.39 for CO_2 , and 0.98 for CH_4 , all those values having been estimated using Cantera). All other thermodynamic and transport properties (e.g., density ρ_k , specific enthalpy h_k , specific heat capacity at constant pressure $C_{p,k}$ and at constant volume $C_{v,k}$, heat diffusion coefficient λ_k , and dynamic viscosity μ_k of each species k) are interpolated from the NIST database³⁷ through lookup tables implemented in DINO. The thermophysical properties (Φ) of the mixture are calculated as

$$\Phi = \sum_k X_k \Phi_k, \tag{6}$$

where X_k and Φ_k are the mole fraction and thermophysical properties of species k , respectively.

To resolve the particle surface, a directional ghost-cell immersed boundary method (IBM)^{38,39} has been employed. In this IBM, the determination of the physical quantities (velocity, temperature, species concentrations, etc.) on the boundary is crucial for the overall accuracy of the boundary representation. In the SCWG process, the solid particle surface reacts with the incoming supercritical water and generates gases from the interface. The gases are then released, resulting in an outgoing flow from the particle to the main stream, known as Stefan flow. The Stefan velocity \mathbf{u}_S satisfies the mass conservation law on the interface as

$$\mathbf{u}_S \cdot \mathbf{n} = \frac{1}{\rho} \sum_{k=1}^{N_g} \dot{\omega}_k, \tag{7}$$

TABLE I. Kinetic parameters describing the gasification mechanism of PP plastic waste in supercritical water. A [for surface reaction: in s^{-1} ; for gaseous reaction: in $cm^3/(mol\ s)$] is the pre-exponential factor, and E_a (in J/mol) is the activation energy.

n	Reactions	A	E_a
1	$PP(C_3H_6) + H_2O \rightleftharpoons 2CH_4 + CO$	$3.418\ 477 \times 10^4$	$1.400\ 873 \times 10^5$
2	$PP(C_3H_6) + 6H_2O \rightleftharpoons 3CO_2 + 9H_2$	$3.312\ 707 \times 10^{-2}$	$4.366\ 236 \times 10^4$
3	$PP(C_3H_6) + 3H_2O \rightleftharpoons 3CO + 6H_2$	$2.453\ 34 \times 10^3$	$1.533\ 64 \times 10^5$
4	$PP(C_3H_6) + 3H_2 \rightleftharpoons 3CH_4$	$1.131\ 994 \times 10^{-1}$	$2.136\ 867 \times 10^4$
5	$PP(C_3H_6) + 4H_2O \rightleftharpoons CH_4 + 2CO_2 + 5H_2$	$4.252\ 702 \times 10^{10}$	$2.883\ 95 \times 10^5$
6	$CO + H_2O \rightleftharpoons CO_2 + H_2$	$3.157\ 576 \times 10^{13}$	$2.405\ 24 \times 10^5$

where N_g is the total number of gaseous species on the particle surface and \mathbf{n} is the wall normal direction on the surface. Due to the surface reactions and consumption of the solid particle, the particle shrinks with velocity,

$$\mathbf{u}_n \cdot \mathbf{n} = \frac{\oint_{surf} \dot{\omega}_{solid} ds}{\pi r_s \rho_{solid}}, \quad (8)$$

where $\dot{\omega}_{solid}$ is the mass consumption rate of the solid particle, r_s is the radius of the solid particle, and ρ_{solid} is the solid density. Due to the reaction, the radius of the solid particle changes by an amount $\Delta r_s = \mathbf{u}_n \cdot \mathbf{n} \Delta t$ during time step Δt . This moving boundary condition is captured and modeled using the implemented, directional ghost-cell IBM.^{38,39} Finally, the velocity at the solid particle surface is given as

$$\mathbf{u}_b = \mathbf{u}_s + \mathbf{u}_n. \quad (9)$$

The particle surface temperature is balanced by the heat release from the surface reactions and heat conduction from the surrounding gases. Since heat conduction within the solid is outside of scope of the present study, we assume that the particle has a low Biot number, following previous studies.²² This leads to a uniform temperature within the solid and is appropriate for sufficiently small particles and/or materials with high heat conductivity. Since the present study only considers particles much smaller than 1 mm, this assumption should be valid. Finally, the following equation is solved for surface temperature T_b ,

$$\frac{dT_b}{dt} = \frac{1}{\rho_{solid} V c_{solid}} \oint_{surf} \left(\sum_{k=1}^{N_k} h_k \dot{\omega}_k + \mathbf{n} \cdot \lambda \Delta T|_{surf} \right) ds, \quad (10)$$

where $V = \frac{4}{3} \pi r_s^3$ is the volume of the spherical particle and c_{solid} is the specific heat capacity of the solid particle. The balance equation for the mass fraction of the gaseous species Y_k on the particle surface is

$$\mathbf{u}_b \cdot Y_k = \frac{\dot{\omega}_k}{\rho} - \mathbf{n} \cdot D_k \Delta Y_k|_{surf}, \quad (11)$$

where D_k is the diffusion coefficient of species k . After incorporating these balance equations in the IBM, the particle surface is fully resolved in the numerical model. A detailed validation of this PR-DNS procedure has already been documented in our previous studies.^{20,21,39}

B. Chemical kinetics of PP

It is first necessary to check the validity of chemical kinetics to describe surface and gaseous reactions in the PR-DNS. The focus of

the present study is set on SCWG of PP particles. The chemical kinetics measured by Bai *et al.*⁶ in a recent experimental study has been slightly adapted in this work, as shown in Table I. The PP plastic waste is first simplified as a collection of C_3H_6 monomers. Reactions 1–5 in Table I belong to surface reactions, while reaction 6 takes place in the gas phase. It is further assumed that all surface reactions are first-order reactions. For these surface reactions, the amount of water involved is unknown. Since the amount of water available in the system is extremely large compared to the consumption, the water concentration is assumed to be constant. Additionally, the solid particle is considered homogeneous, without any gradient of temperature or composition. After including all those assumptions in the model, the resulting kinetics for SCWG of PP listed in Table I has been validated, as documented in Fig. 1. It can be seen that the resulting PP plastic consumption and gas production rates obtained with our kinetic model match very well with the experimental measurements in Bai *et al.*⁶ In the original kinetic mechanism of Bai *et al.*,⁶ C_2H_2 is an important intermediate species, produced by the fast pyrolysis reaction [$PP(C_3H_6) \rightleftharpoons CH_4 + C_2H_2$]. However, due to the short lifetime of C_2H_2 in the experiments, there is no accurate thermodynamic description for this intermediate species under SCWG conditions. Therefore,

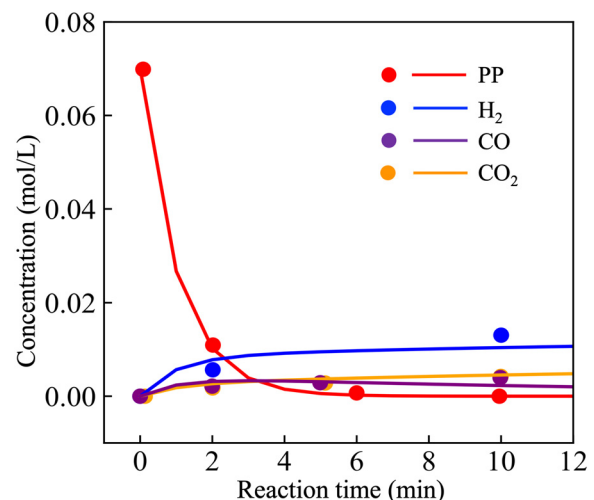


FIG. 1. Validation of the kinetic mechanism listed in Table I for PP plastic waste gasification in supercritical water. Solid lines: predicted data; symbols: experimental results from Bai *et al.*⁶ Conditions: temperature: 650 K and pressure: 23 MPa.

TABLE II. Kinetic parameters¹⁴ for the gasification mechanism of coal particle in supercritical water. A [for surface reaction: in s⁻¹; for gaseous reaction: in cm³/(mol s)] is the pre-exponential factor, and E_a (in J/mol) is the activation energy.

N	Reactions	A	E _a
1	C + H ₂ O ⇌ CO + H ₂	4.727 33 × 10 ⁻⁶	2.776 × 10 ⁴
2	C + 2H ₂ O ⇌ CO ₂ + 2H ₂	3.835 883 × 10 ³	1.7664 × 10 ⁵
3	CO + H ₂ O ⇌ CO ₂ + H ₂	2.275 67 × 10 ⁴	9.683 × 10 ⁴

it is currently not possible to include this fast pyrolysis reaction as a standalone reaction in the model. In the adapted mechanism (shown in Table I), we have combined the fast pyrolysis reaction with the following slow reaction (C₂H₂ + H₂O ⇌ CH₄ + CO) into reaction 1 [PP(C₃H₆) + H₂O ⇌ 2CH₄ + CO]. This treatment results in underestimation of CH₄ in some extents (around 40%) by this updated mechanism. Since CH₄ is not involved in any reaction rate of the other (surface or gaseous) reactions, differences regarding CH₄ concentration will not lead to any error propagation. As observed in Fig. 1, the prediction of all other species using the adapted kinetic of Table I is excellent.

To understand better the SCWG process of the PP plastic, the SCWG of coal particle is considered for comparison, since the latter is a configuration considered in many recent studies. The chemical kinetics of coal particle gasification in supercritical water from Ref. 14 has been used in the present study, as listed in Table II. Reactions 1–2 are surface reactions, while reaction 3 is a gaseous reaction. Note that the gaseous reactions for PP plastic and coal in Tables I and II are the same, but with different reaction rate parameters, as obtained from the corresponding references.

C. Numerical configuration

The numerical configuration of the PR-DNS is sketched in Fig. 2. The computational domain is 18 D × 12 D—sufficiently large to prevent any influence from the boundary conditions, where D = 500 μm is the initial diameter of the spherical solid particle, typical for particles

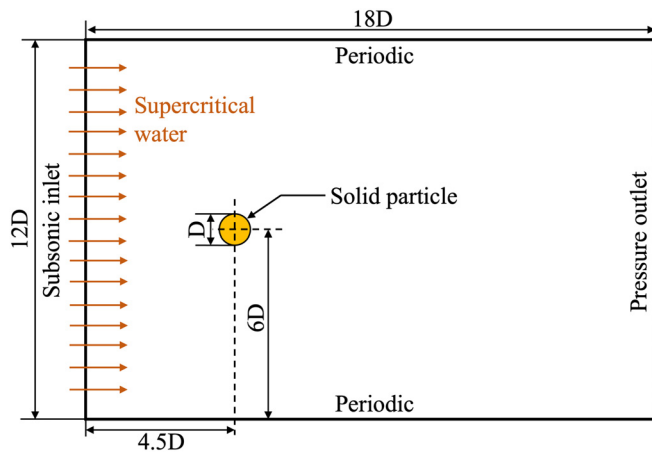


FIG. 2. Numerical configuration considered for PR-DNS.

in practical SCWG processes involving coal. The domain is uniformly discretized by 600 × 400 grid points, ensuring a sufficient accuracy.

Three kinds of particles are considered in supercritical water: (1) inert particle, (2) coal particle, reacting according to Table II, and (3) PP particle, reacting according to Table I. The flow is simulated at a particle Reynolds number (Re = ρU_∞D/μ, where U_∞ is the inflow velocity) of 5, 10, 20, 30, and 40. The operational range of practical SCWG for coal is up until now limited to a maximum Reynolds number around 40 (Ref. 40). The particles are fixed in the domain (no change in position) but are allowed to shrink. The flow is set at a temperature T = 900 K, which is the same as the initial particle temperature. The pressure is set at 25 MPa, corresponding to supercritical condition for water. This temperature and pressure correspond to the practical condition for SCWG application.^{41–43} All the reactive cases have been run for 1 s of physical time and the non-reactive cases for 0.5 s. This is sufficient to reach quasi-steady state for the flow. The simulation time step is simultaneously controlled by the Courant–Friedrichs–Lewy (CFL) number (set at a maximum of 0.1) and the Fourier number (again, limited to 0.1), resulting in a typical time step Δt of about 10 μs.

Similar to the study published in Ou et al.,²⁰ the impact of resolution has been investigated using the velocity distributions along the radial direction at θ = 60° as a function of non-dimensional distance L/D, as plotted in Fig. 3. Simulations are compared for an inert particle using 600 × 400 grids and for a reacting PP particle using either 600 × 400, 300 × 200, or 150 × 100 grid points, for a flow at particle Reynolds number equal to 40. As is seen, the orange (300 × 200) and blue curves (600 × 400) show convergence, while the results obtained on a 150 × 100 grid strongly deviate from the finer solutions. This confirms that the finally retained resolution (600 × 400 grids) is fully sufficient for the present study. The deviation observed in Fig. 3 between inert particle and reacting PP particle is mainly due to the Stefan flow, as already explained in Ou et al.²⁰

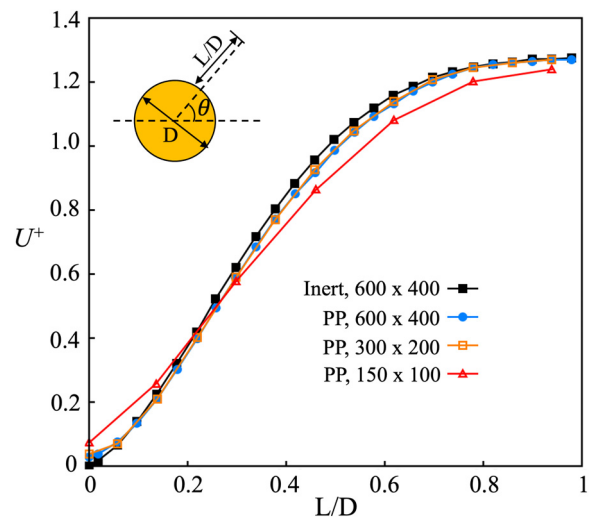


FIG. 3. Radial velocity U⁺ away from the particle surface at θ = 60°, showing the simulations with an inert particle using 600 × 400 grids, compared to a reacting PP particle using either 600 × 400, 300 × 200 grids, or 150 × 100 grids; the blue and orange curves overlap, demonstrating that the two finest resolutions deliver identical results.

III. RESULTS AND DISCUSSION

In this section, the results of the PR-DNS are analyzed in detail. Note that the results are always analyzed after reaching quasi-steady state. The changes in temperature are also very small due to the slow reactions. Therefore, the effect of changing fluid properties is negligible in this case. First, the interphase momentum transfer is considered, revealing the main flow characteristics for the SCWG process. Then, interphase heat and mass transfer are investigated, in order to check the dominating thermochemical process on the particle surface. Finally, the impact of chemical reactions is investigated, which is important to understand SCWG of PP plastic particles in real conditions.

A. Interphase momentum transfer

The flow over a 2D inert particle has already been extensively investigated in the last few decades. The flow starts to separate and form two symmetrical vortices in the wake at around $Re = 7$; these vortices become unsteady, generating periodic Kármán vortex streets at around $Re = 47$ (Ref. 44) (beyond the highest Reynolds number considered in the present study). Figure 4 shows the streamlines of the flow field around an inert particle, a coal particle (with reactions following Table II), and a PP plastic particle (with reactions following Table I), at $Re = 5$ (left) and 40 (right). The flow field for the inert particle is as expected, with no separation of the flow at $Re = 5$, and two stable symmetrical vortices found in the wake at $Re = 40$.

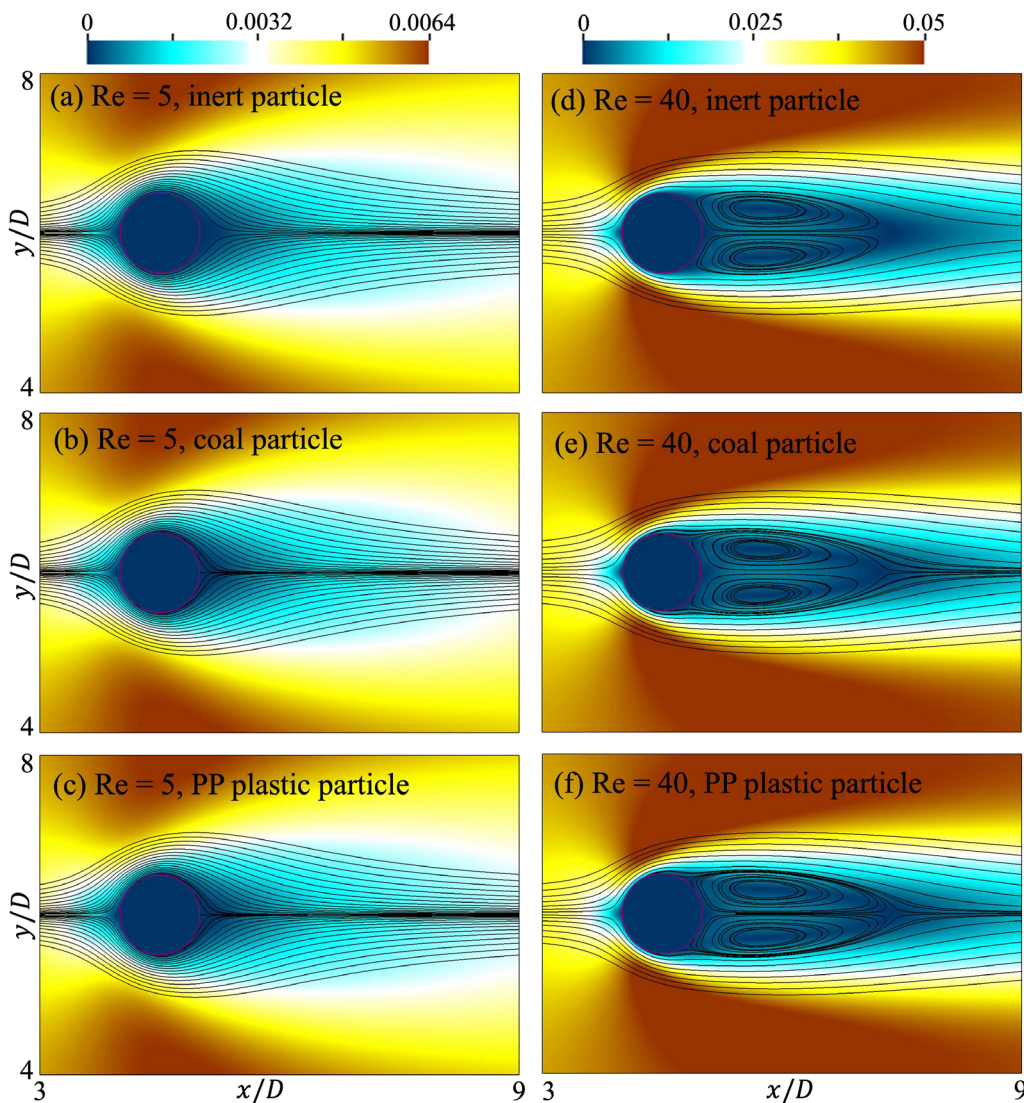


FIG. 4. Streamlines of the flow field together with a color plot showing the velocity magnitude (in m/s) for PR-DNS of the flow of supercritical water: around an inert particle (a) and (d); around a coal particle [with reactions following Table II] (b) and (e); around a PP plastic particle [with reactions following Table I] (c) and (f). Results are compared for a particle Reynolds number of $Re = 5$ (left) and 40 (right).

The recirculation length at $Re = 40$ is $2.28D$, matching well results from the literature.^{45,46} The flow fields around the coal particle and PP plastic particle appear to be only slightly different from that of the inert particle. Looking now more closely around the particle, streamlines emerging from the particle surface are seen for coal and PP (this is better visible at $Re = 40$), revealing the existence of a Stefan flow. This Stefan flow pushes the incoming flow away from the particle, extending the boundary layer. Due to this, the vortical structures downstream of the particles are slightly modified, and the recirculation lengths are extended a bit, to $2.30D$ for coal and $2.32D$ for PP particle. The changes are relatively small, since the surface reactions are slow for both the coal and PP plastic particles. The Reynolds number of the Stefan flow is computed as $Re_{Stefan} = \rho U_{Stefan} D / \mu$. In the present simulation, the Stefan flow for the coal particle corresponds to $Re_{Stefan} = 1.12 \times 10^{-6}$, and for the PP particle, it corresponds to $Re_{Stefan} = 6.48 \times 10^{-3}$. Note that the Stefan flow only depends on the surface reactions, as described in Eq. (7). Therefore, Re_{Stefan} is independent from the incoming flow Reynolds number.

A very important quantity to quantify interphase momentum transfer is the drag coefficient. The overall drag coefficient Cd can be decomposed into pressure coefficient Cd_p and friction coefficient Cd_f , defined as,

$$Cd_p = \frac{\oint p n_x ds}{0.5 \rho U_\infty^2 D}, \tag{12}$$

$$Cd_f = \frac{-\oint \mu [\nabla \mathbf{u} + (\nabla \mathbf{u})^T] \mathbf{n}_x ds}{0.5 \rho U_\infty^2 D} \tag{13}$$

using the upstream velocity U_∞ for normalization. Figure 5 shows the pressure coefficient and friction coefficient for the inert particle, reacting coal particle, and reacting PP particle as a function of Reynolds number. The reference solution from Ref. 44 for an inert particle is also plotted for comparison. The present study for the inert particle matches perfectly with the reference, confirming the high accuracy obtained in this work. Overall, both the pressure coefficient and friction coefficient decrease rapidly as the Reynolds number increases. Compared with the inert particle, the reacting coal particle shows a slightly larger Cd_p and smaller Cd_f . This is due to the outgoing Stefan flow, as also found in Refs. 18 and 19. The difference is more obvious at smaller Reynolds numbers, since the relative influence of the Stefan flow increases when the incoming flow is weaker (lower U_∞ , hence lower Re). The reacting PP plastic particle shows even larger Cd_p and smaller Cd_f , compared to the coal particle. This is because the surface reactions for PP are slightly more intensive than for coal, thus generating larger Stefan flow velocity (with larger Re_{Stefan}), as already visible in Fig. 4 from the somewhat longer recirculation zone.

B. Interphase heat transfer

After checking interphase momentum transfer, it is now interesting to analyze interphase heat transfer. The heat transfer efficiency can be best quantified by the Nusselt number,

$$Nu = \frac{\oint \nabla T \cdot \mathbf{n} ds}{T_{solid} - T_\infty}, \tag{14}$$

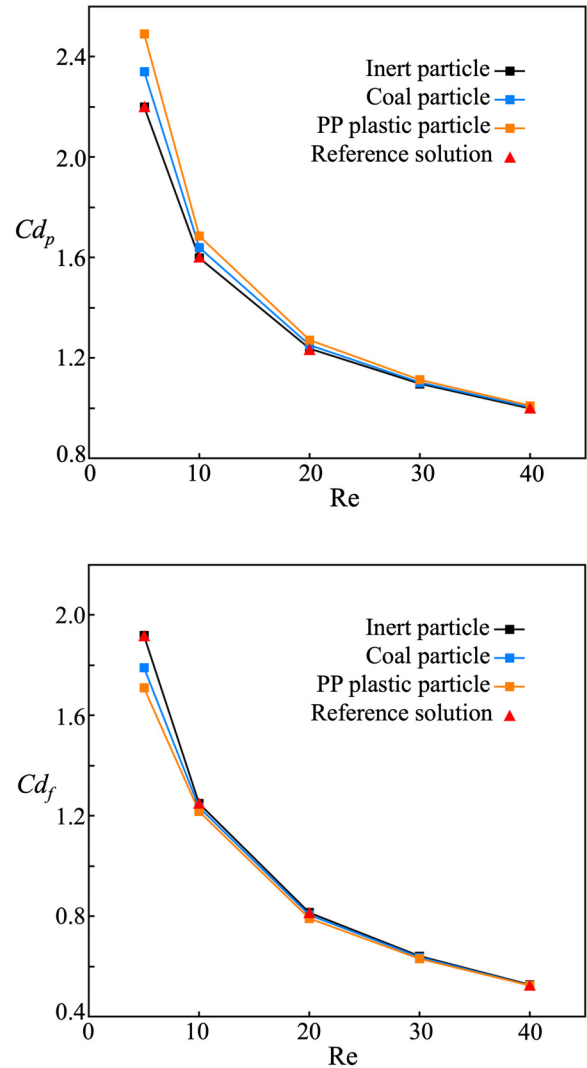


FIG. 5. Drag coefficient (top: pressure coefficient; bottom: friction coefficient) vs Reynolds number for the inert particle (black), reacting coal particle (blue), and PP plastic particle (orange). The reference solution from Ref. 44 for an inert particle is also plotted with red triangles.

where T_{solid} is the solid temperature and T_∞ is the inflow temperature. Since in the current study the same temperature has been initially imposed to the particle and the surrounding flow, there is no heat transfer for the inert particle. Therefore, a reference solution based on the well-known Churchill–Bernstein correlation⁴⁷ has been used to calculate the Nusselt number for an inert particle,

$$Nu = 0.3 + \frac{0.62 Re^{1/2} Pr^{1/3}}{[1 + (0.4/Pr)^{2/3}]^{1/4}} \left[1 + \left(\frac{Re}{28200} \right)^{5/8} \right]^{4/5}, \tag{15}$$

where $Pr = \mu C_p / \lambda$ is the Prandtl number (equal to 0.985 for supercritical water in the present conditions).

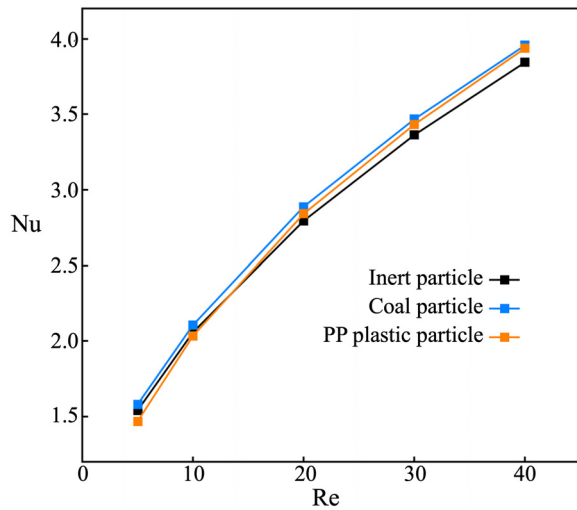


FIG. 6. Nusselt number vs Reynolds number for an inert particle (Churchill–Bernstein correlation, in black), reacting coal particle (blue), and reacting PP plastic particle (orange).

Figure 6 shows the Nusselt number for the inert particle (from the correlation) and for the reacting coal particle and PP particle (from the PR-DNS simulations) at different Reynolds numbers. Overall, the Nusselt number is increasing as the Reynolds number increases, as expected. This is because the thermal boundary layer becomes thinner as the Reynolds number increases. Compared to the inert particle, the Nusselt number for the coal particle is always larger. Due to the chemical reactions, there are two factors influencing heat

transfer in two different directions: (1) heat release due to the gaseous reactions increases the temperature near the particle surface, thus affecting the temperature gradient there and increasing Nusselt number; (2) the Stefan flow expands the thermal boundary layer, resulting in a smaller Nusselt number. In fact, the situation is slightly more complex, since the surface reactions are endothermic reactions, while only the gaseous reactions are exothermic; this is typical for most SCWG processes. Overall, the heat release due to the gaseous reactions dominates, finally increasing the temperature gradient near the particle surface and resulting in a larger Nusselt number, as stated previously. The competition between these two factors leads to a complex trade-off regarding heat transfer. For the coal particle, at $Re = 5$, the heat transfer enhancement by the gaseous reaction is only slightly more intensive than the contrary effect induced by the Stefan flow, so that Nu is only very slightly larger than for the inert particle. At $Re = 40$, the relative effect of the Stefan flow weakens, so that the relative increase in Nusselt number is much clearer, by 3%. For PP at $Re = 5$, the Stefan flow is dominating, leading to a slightly lower Nu compared to the inert particle. Again, at higher Reynolds numbers, the influence of the Stefan flow becomes weaker, and heat release induced by the gaseous reaction dominates, so that the Nusselt number for PP particle exceeds that of the inert particle for $Re \geq 20$. The different behavior between coal and PP particle is mainly due to the somewhat faster (endothermic) surface reactions for PP.

The difference between the Nusselt numbers of coal particle and PP plastic particle can be also derived from Fig. 7, in which the temperature field and contours around the particle are plotted. The temperature is normalized as

$$T^+ = \frac{T - T_{solid}}{T_{\infty} - T_{solid}}. \quad (16)$$

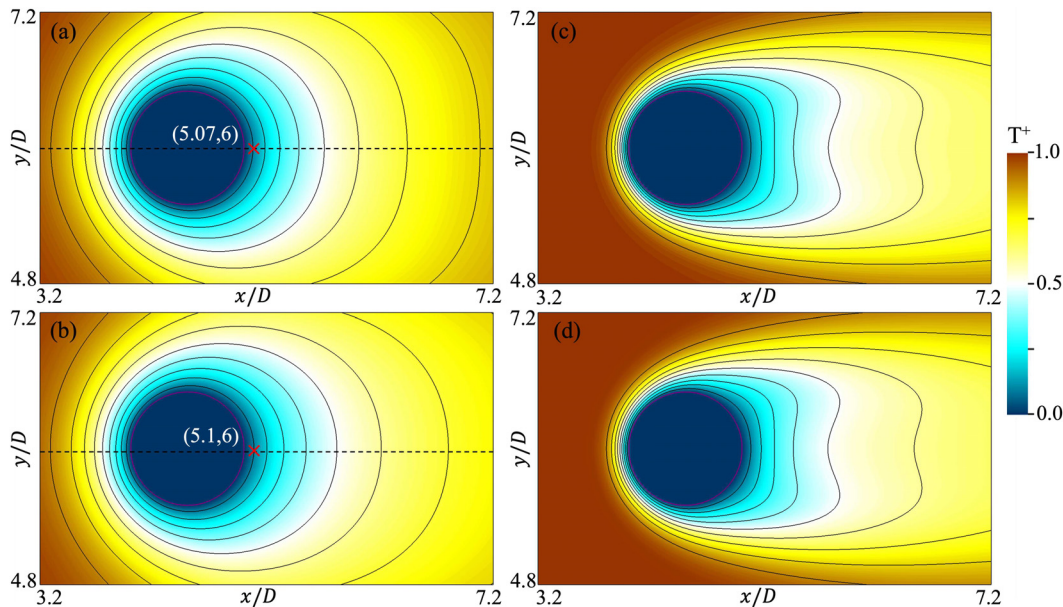


FIG. 7. Temperature (color plot) around the reacting coal particle (top) at $Re = 5$ (a) and $Re = 40$ (c); the PP plastic particle (bottom) at $Re = 5$ (b) and $Re = 40$ (d). The additional isocontour lines in black indicate $T^+ = 0.1-0.9$, going away from particle surface. The particle boundary is shown with a red line.

As is seen, the isocontour line $T^+ = 0.1$ (as well as all other ones) is closer to the particle surface for coal at $Re = 5$ on the downstream side. The difference is perhaps even more visible looking at the yellow color, which extends much farther downstream of the PP particle [Fig. 7(b)]. On the other hand, the temperature fields are very similar for coal and PP at $Re = 40$. This is consistent with the results in Fig. 6 (almost identical Nusselt numbers there).

C. Interphase mass transfer

Finally, it is also crucial to analyze interphase mass transfer. The mass transfer intensity of any species k can be characterized by the Sherwood number:

$$Sh = \frac{\oint \nabla Y_k \cdot \mathbf{n} ds}{Y_{k,surf} - Y_{k,\infty}}, \quad (17)$$

where $Y_{k,surf}$ is the averaged mass fraction of species k on the particle surface,

$$Y_{k,surf} = \frac{\oint Y_k ds}{\pi D} \quad (18)$$

and $Y_{k,\infty}$ is the mass fraction of species k in the inlet flow. Obviously, the inert particle is not associated with any reaction, and the corresponding simulation cannot be used to derive Sherwood numbers. Again, a reference solution based on the well-known Churchill–Bernstein correlation⁴⁸ has been used as an alternative to calculate the Sherwood number for an inert particle,

$$Sh = 0.3 + \frac{0.62Re^{1/2}Sc^{1/3}}{\left[1 + (0.4/Sc)^{2/3}\right]^{1/4}} \left[1 + \left(\frac{Re}{28200}\right)^{5/8}\right]^{4/5}, \quad (19)$$

where $Sc = \mu/(\rho D_k)$ is the Schmidt number for species k [replacing the Prandtl number appearing in Eq. (15)]. Note that $Sc = Le_k Pr$, where Le_k is the effective Lewis number of species k . For the present conditions, Le_k is calculated using Cantera to be 0.29 for H_2 , 1.09 for CO, 1.39 for CO_2 , and 0.98 for CH_4 . Since Pr is always equal to 0.985, the finally calculated Sherwood number is also different for different species, even in the non-reacting case.

Figure 8 shows the Sherwood number of H_2 , CO, CO_2 , and CH_4 for the inert particle (from the correlation), reacting coal and PP particles (from the PR-DNS simulations) as a function of particle Reynolds number. Overall, the Sherwood number is increasing as the Reynolds number increases, due to the thinning species boundary layer at higher Reynolds number, similar to the evolution of the Nusselt number. Looking first at the inert particle, it is visible that the Sherwood number is much smaller for H_2 and larger for CO_2 . This is because H_2 has a much smaller Lewis number, resulting in a faster molecular diffusion—the hydrogen molecule is small and very mobile. This leads to a smaller species gradient near the surface, reducing the Sherwood number. Even for the reacting particles, this effect is visible, and the Sherwood number of H_2 is always the smallest one. However, compared to the inert case, the reactive cases are far more complicated due to the competing effects of reactions and Stefan flow. The Stefan flow expands the species boundary layer, leading to a smaller

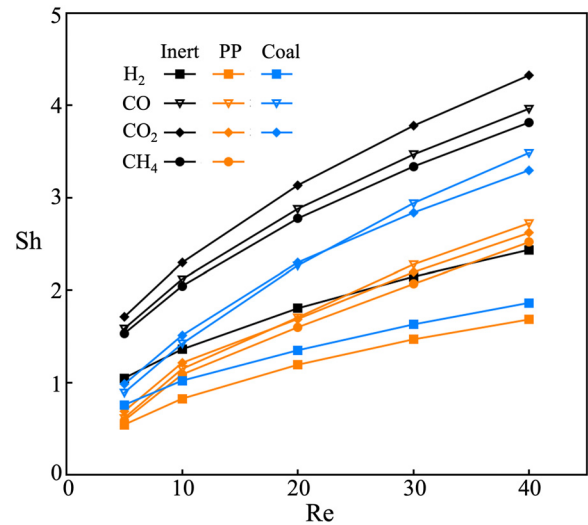


FIG. 8. Sherwood number of H_2 , CO, CO_2 , CH_4 vs Reynolds number for the inert particle (black), reacting coal particle (blue), and reacting PP particle (orange).

Sherwood number. The gaseous reaction consumes CO and produces CO_2 and H_2 , resulting in a larger Sherwood number for CO and smaller Sherwood numbers for CO_2 and H_2 .

Looking first at the reacting coal particle, the Sherwood numbers for all gaseous species are smaller than for the inert case. This indicates that the effect of the Stefan flow dominates over chemical reactions for the range of Reynolds numbers considered here. Still, the relative importance of the reactions increases with Reynolds number, explaining why the Sherwood number of CO exceeds that of CO_2 for $Re \geq 30$. Regarding now PP plastic particle, the Sherwood numbers are even smaller than for the coal particle, due to the faster surface reactions. Here also, the relative importance of the Stefan flow diminished with the Reynolds number, so that reaction effects increasingly dominate. For this reason, the Sherwood number of CO starts exceeding that of CO_2 soon after $Re = 20$. While all Sherwood numbers lie close to each other at particle Reynolds number of 5, there is almost a factor of two between the largest one (for CO_2) and the smallest one (for H_2) at $Re = 40$.

The change in the Sherwood number for different species at different Reynolds numbers can also be understood by looking at Fig. 9 for the coal particle and at Fig. 10 for the PP plastic particle. These two figures show one selected species isocontour for different species at four different Reynolds numbers. Here, the mass fraction of species k has been normalized using

$$Y_k^+ = \frac{Y_k - Y_{k,surf}}{Y_{k,\infty} - Y_{k,surf}} \quad (20)$$

using the averaged species mass fraction at the particle surface (index surf) and in the inflow (index ∞). As is seen in Figs. 9 and 10 (note the different scales of the two color bars), the thinning of the species boundary layer when increasing Reynolds number as a consequence of stronger convection is obvious. The minimum species gradient around the particle is always located in the wake region. As the Reynolds number increases, the difference between the isocontours of

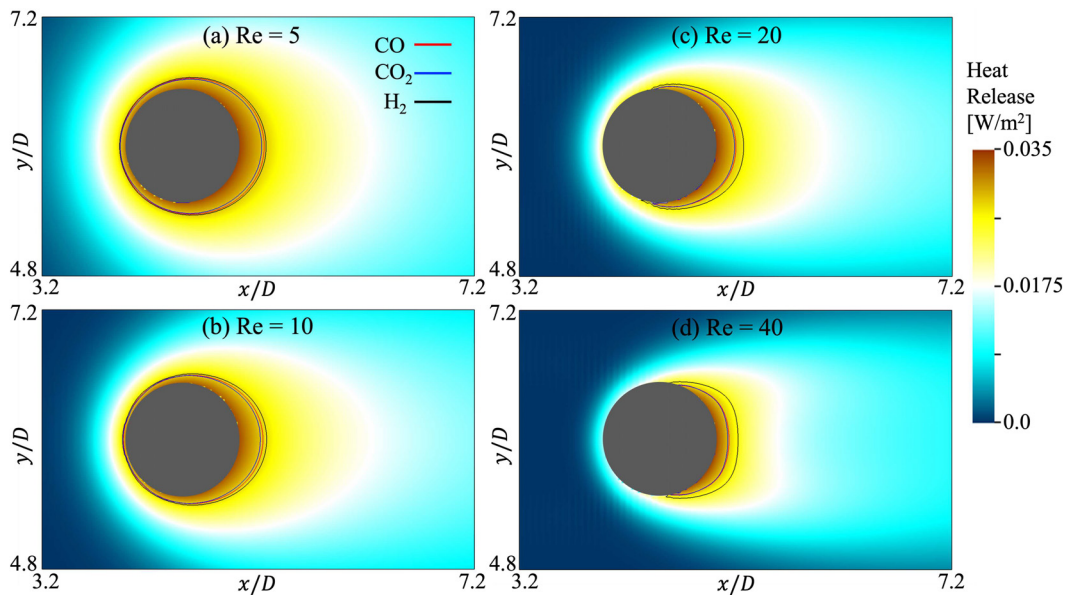


FIG. 9. Species isocontours $Y_k^+ = 0.2$ at (a) $Re = 5$, (b) $Re = 10$, (c) $Re = 20$, and (d) $Re = 40$ for the reacting coal particle. The color plot shows the heat release in the gas phase, and the surface heat release is not shown here.

H_2 and CO/CO_2 becomes larger, confirming the larger difference between the corresponding Sherwood numbers at higher Reynolds numbers in Fig. 8. Compared to the coal particle, the species boundary layer is thinner for the PP plastic particle, especially at higher Reynolds number. The gaseous reaction (releasing heat) is limited to the immediate vicinity of the particle at $Re = 40$ and is far more

intensive in this wake region; the reaction heat release around the PP plastic particle is about 4 orders of magnitude larger than around the coal particle. Compared to coal, the released gases are more concentrated in the wake region for PP at $Re = 40$. This might be advantageous for subsequent gases collection in a SCWG process involving PP.

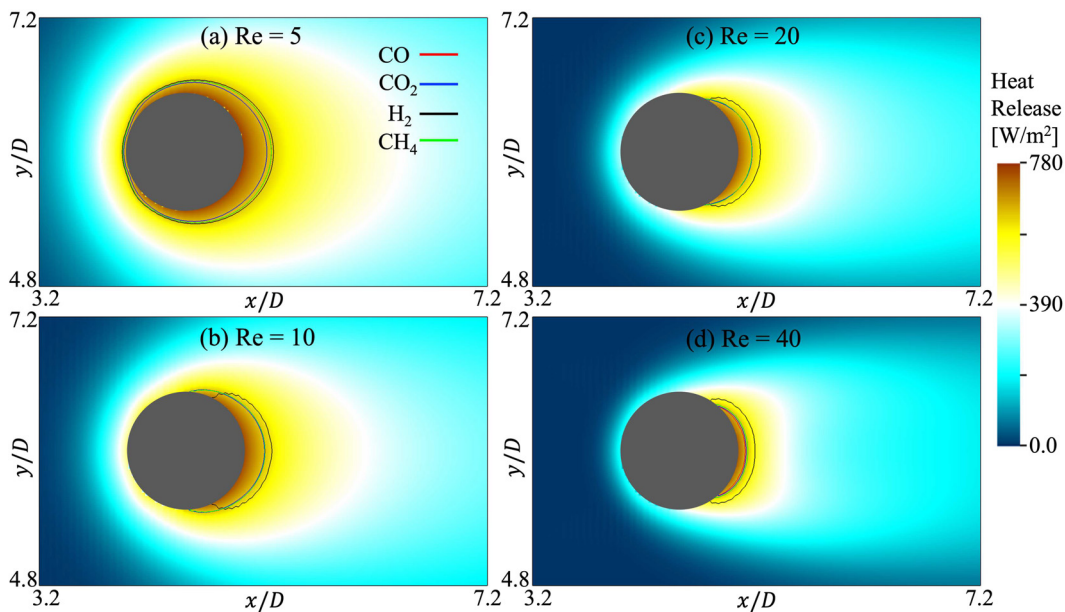


FIG. 10. Species isocontours $Y_k^+ = 0.2$ at (a) $Re = 5$, (b) $Re = 10$, (c) $Re = 20$, and (d) $Re = 40$ for the reacting PP particle. The color plot shows the heat release in the gas phase, and the surface heat release is not shown here.

D. Chemical reactions

Since the interphase heat and mass transfer are highly related to the chemical reactions, it is finally necessary to get a deeper understanding of the surface and gaseous reactions. The surface reactions generate gaseous products around the particle. Figure 11 shows the surface-averaged mass fraction of these gaseous species on the coal particle and PP plastic particle as a function of Reynolds number. For both cases, CO₂ is the most important product on the surface. The mass fractions of all gaseous species decrease as the Reynolds number increases, due to the enhanced mass transfer discussed in Sec. III C. Since the surface reactions are much faster for the PP plastic particle, the mass fractions of all gaseous species are larger, compared to coal. The total gas production speed of the PP plastic particle is roughly three orders of magnitude larger than for the coal particle, demonstrating the very efficient gasification performance for PP plastic particles.

Now, the surface reaction rates are directly evaluated for the coal and PP particle, as shown in Fig. 12, revealing the variation of the individual reaction rates with the initial surface temperature (same as the initial flow temperature). For PP, the reaction rates of reactions 1 and 2 are much faster than the other surface reactions. The reaction rates of all surface reactions increase as the temperature increases, with reactions 1, 3, and 5 being most sensitive to a change in temperature change. At lower temperatures, reaction 2 [PP(C₃H₆) + 6H₂O ⇌ 3CO₂ + 9H₂] is dominating, producing most of CO₂ and H₂. Above about 850 K, reaction 1 [PP(C₃H₆) + H₂O ⇌ 2CH₄ + CO] becomes dominating and controls the production of CH₄ and CO.

Regarding now the coal particle, reaction 1 is dominating at lower temperatures, while reaction 2 takes over shortly before 900 K, becoming the dominant pathway at higher temperatures. As already discussed previously, the surface reaction rates for PP are much higher than those for a coal particle.

Concerning finally the gaseous reaction, the characteristic time-scale of the gaseous reaction τ_{react} is evaluated and compared with the

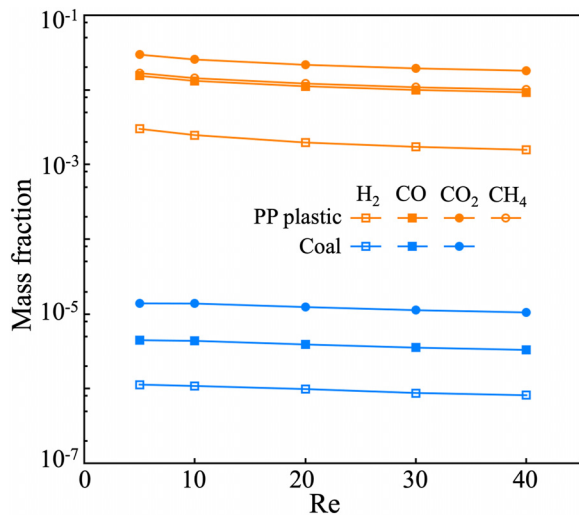


FIG. 11. Surface-averaged mass fraction of the gaseous species on the coal and PP particle surface at different Reynolds numbers.

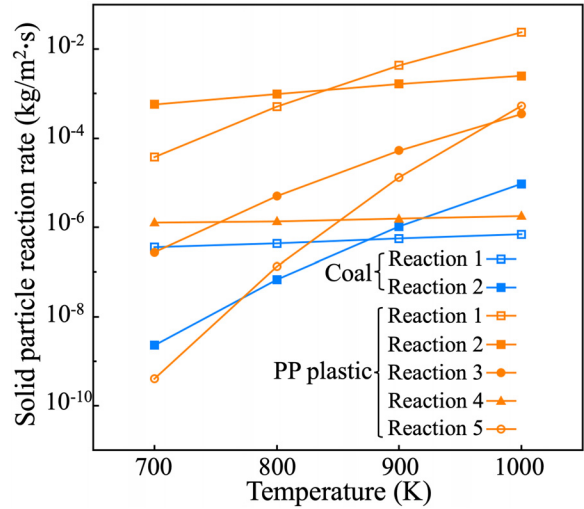


FIG. 12. Surface reaction rates for the coal particle and PP plastic particle at different temperatures.

convection timescale τ_{conv} and diffusion timescale τ_{diff} . Similar to the studies in Ref. 20, the reaction and diffusion time-scales are based on CO, which is mostly considered as an undesired by-product in SCWG processes. Therefore, the time-scales are calculated as

$$\tau_{conv} = \frac{D}{U_{\infty}}, \tag{21}$$

$$\tau_{diff} = \frac{D^2}{D_{CO}}, \tag{22}$$

$$\tau_{react} = \frac{Y_{CO}}{\dot{\omega}_{CO}}, \tag{23}$$

where D_{CO} and $\dot{\omega}_{CO}$ are the diffusion coefficient and mass production rate of CO, respectively. The convective Damköhler number is used to compare the convection timescale and reaction timescale,

$$Da_{conv} = \frac{\tau_{conv}}{\tau_{react}}, \tag{24}$$

and the diffusive Damköhler number is used to compare the diffusion timescale and reaction timescale,

$$Da_{diff} = \frac{\tau_{diff}}{\tau_{react}}. \tag{25}$$

Figure 13 shows these convective and diffusive Damköhler numbers for the coal particle and PP plastic particle at $Re = 40$ at different initial temperatures (same for the flow and particle surface). As is seen, both Da_{conv} and Da_{diff} are considerably smaller than 1, especially at low temperatures. This means that the gaseous reaction is limited by its slow reaction rate, while convection and diffusion processes are very efficient in comparison. By increasing the temperature, both Damköhler numbers are rapidly increasing, due to the faster reaction rate. This effect is even more obvious for the PP plastic particle. This indicates that increasing temperature would be an efficient way to remove CO from the residual gases and would improve the balance between reaction, convection, and diffusion processes.

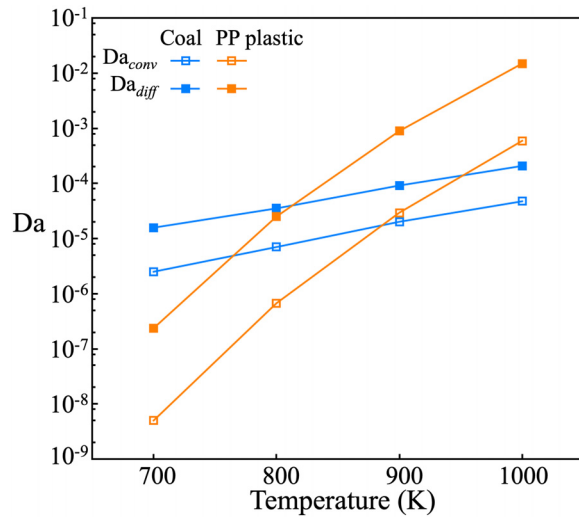


FIG. 13. Convective and diffusive Damköhler numbers for the coal and PP plastic particles at different temperatures.

The effect of species transport on the surface reactions is negligible in this case, since the reactions are first-order reactions, and Y_{H_2O} is much larger than the mass fractions of the other species. However, the impact of species transport on the gaseous reaction is obvious. Compared with a coal particle, the PP particle corresponds to a much faster transport of the gaseous species away from the solid surface, resulting in a higher gaseous reaction rate.

Finally, due to the surface reactions, the solid particle is shrinking with time. The particle shrinkage is quantified as

$$\alpha = \frac{|r - r_{init}|}{r_{init}}, \quad (26)$$

where $r_{init} = 250 \mu\text{m}$ is the initial radius of the particle considered in this study. Figure 14 shows the time evolution of particle shrinkage for the coal particle and PP plastic particle at different initial surface temperatures. Since the surface reactions are basically independent from the incoming flow velocity, due to the small amount of gases generated by comparison to the amount of SCW, the shrinkage speed does not depend on the flow Reynolds number; for Fig. 14, $Re = 40$ has been selected.

As is seen, initial surface temperature very significantly affects the shrinkage speed of PP plastic particles. By comparison, the shrinkage speed of the coal particle is small; even at a temperature of 900 K, it remains much smaller than the shrinkage of a PP particle at a lower temperature of $T = 700 \text{ K}$.

Coming back to PP, the overall particle shrinkage amounts to almost 3% of the initial particle radius during 1 s (duration of the PR-DNS simulation in physical time). Therefore, the quasi-steady state assumption is valid for this condition. Increasing the temperature to $T = 1000 \text{ K}$, the shrinkage level exceeds 10% after 1 s. Going to even higher temperature would increasingly lead to strong transient processes and unsteady flow properties, impacting interphase momentum and heat and mass exchange. Being intrinsically an unsteady solver, DINO is perfectly suitable to investigate such conditions. This will be the subject of future work.

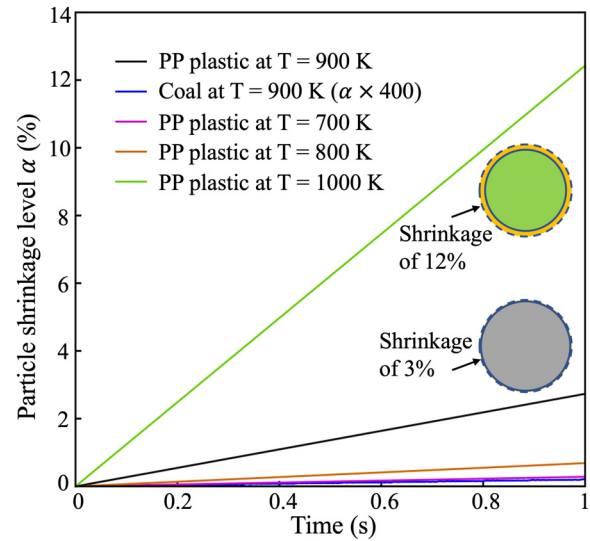


FIG. 14. Time evolution of particle shrinkage level for coal and PP plastic particle at different initial surface temperatures.

IV. CONCLUSIONS

The present study investigates the supercritical water gasification of coal and polypropylene plastic particles in a flow at different Reynolds numbers using particle-resolved direct numerical simulations. In this first step, two-dimensional simulations are considered to reduce the numerical costs. The employed chemical kinetics for coal and PP gasification in supercritical water has been adapted from the literature. Detailed thermodynamic and transport models are used. After analyzing in detail interphase momentum, heat and mass transfer as well as the impact of surface and gaseous chemical reactions, following conclusions are obtained for SCWG of PP:

- Compared to a coal particle, the SCWG of PP plastic particles generates a more intensive Stefan flow, resulting in a somewhat larger pressure coefficient and smaller friction coefficient.
- Heat transfer efficiency is affected by both Stefan flow and gaseous reaction. Compared to a coal particle, the Stefan flow effect is more pronounced for PP, especially at low Reynolds numbers, resulting in a smaller Nusselt number.
- Differential diffusion results in different mass transfer efficiency for each species. The gaseous reaction leads to larger Sherwood number for CO and smaller Sherwood number for CO₂ and H₂. The Sherwood numbers are always smaller for PP particles compared to coal during SCWG.
- Again compared to a coal particle, the produced gases are more concentrated in the wake region of the PP particle at higher Reynolds number, facilitating residual gases collection in a practical SCWG process.
- Due to faster surface reactions, SCWG of PP plastic particles produces more than 1000 times as much combustible gas, compared to a coal particle.
- The surface reactions of PP are very sensitive to temperature. At lower temperatures, more CO₂ and H₂ are produced, while at higher temperatures, more CH₄ and CO are produced. At the

same time, when increasing the temperature, CO will be increasingly converted by the gaseous reaction.

- Increasing temperature leads to a rapid increase of convective and diffusive Damköhler numbers, though they remain far below one even at $T=1000$ K. Controlling process temperature appears to be important and promising.

In summary, this study provides a first detailed understanding of SCWG for a PP plastic particle. In practical applications, many particles in fluidized bed reactors with particle volume fractions up to 0.6 and Stokes numbers ranging typically from 1 to 100 will be involved. The effect of neighboring particles on flow field and heat and mass transfer efficiency is expected to be very significant under such conditions. This highlights the need for further PR-DNS studies involving many particles in future studies. Combined with additional findings from the literature, this will hopefully guide the development of practical, large-scale plastic waste recycling systems relying on the SCWG technology.

ACKNOWLEDGMENTS

The authors gratefully acknowledge the Gauss Centre for Supercomputing e.V. (www.gauss-centre.eu) for funding this project by providing computing time through the John von Neumann Institute for Computing (NIC) on the GCS Supercomputer JUWELS at Jülich Supercomputing Centre (JSC). The research of C. Chi and D. Thévenin is part of the Research Initiative “SmartProSys: Intelligent Process Systems for the Sustainable Production of Chemicals” funded by the Ministry for Science, Energy, Climate Protection and the Environment of the State of Saxony-Anhalt.

AUTHOR DECLARATIONS

Conflict of Interest

The authors have no conflicts to disclose.

Author Contributions

Cheng Chi: Conceptualization (equal); Data curation (equal); Formal analysis (lead); Investigation (lead); Methodology (equal); Software (equal); Validation (lead); Visualization (lead); Writing – original draft (lead). **Wei Guan:** Data curation (equal); Formal analysis (equal); Validation (equal); Writing – review & editing (equal). **Zhisong Ou:** Data curation (equal); Methodology (equal); Software (equal); Writing – review & editing (equal). **Kai Sundmacher:** Funding acquisition (equal); Project administration (equal); Writing – review & editing (equal). **Dominique Thévenin:** Conceptualization (equal); Funding acquisition (equal); Project administration (equal); Resources (equal); Supervision (equal); Writing – review & editing (equal).

DATA AVAILABILITY

The data that support the findings of this study are available from the corresponding author upon reasonable request.

REFERENCES

- R. C. Thompson, C. J. Moore, F. S. vom Saal, and S. H. Swan, “Plastics, the environment and human health: Current consensus and future trends,” *Philos. Trans. R. Soc. London Ser. B* **364**, 2153–2166 (2009).
- J. A. Onwudili and P. T. Williams, “Catalytic supercritical water gasification of plastics with supported RuO₂: A potential solution to hydrocarbons–water pollution problem,” *Process Saf. Environ. Prot.* **102**, 140–149 (2016).
- B. Bai, Y. Liu, Q. Wang, J. Zou, H. Zhang, H. Jin, and X. Li, “Experimental investigation on gasification characteristics of plastic wastes in supercritical water,” *Renewable Energy* **135**, 32–40 (2019).
- K. Li and Z. Xu, “A review of current progress of supercritical fluid technologies for e-waste treatment,” *J. Cleaner Prod.* **227**, 794–809 (2019).
- Y. Liu, C. Fan, H. Zhang, J. Zou, F. Zhou, and H. Jin, “The resource utilization of abs plastic waste with subcritical and supercritical water treatment,” *Int. J. Hydrogen Energy* **44**, 15758–15765 (2019).
- B. Bai, W. Wang, and H. Jin, “Experimental study on gasification performance of polypropylene (PP) plastics in supercritical water,” *Energy* **191**, 116527 (2020).
- B. Bai, Y. Liu, X. Meng, C. Liu, H. Zhang, W. Zhang, and H. Jin, “Experimental investigation on gasification characteristics of polycarbonate (PC) microplastics in supercritical water,” *J. Energy Inst.* **93**, 624–633 (2020).
- L. Guo and H. Jin, “Boiling coal in water: Hydrogen production and power generation system with zero net CO₂ emission based on coal and supercritical water gasification,” *Int. J. Hydrogen Energy* **38**, 12953–12967 (2013).
- O. Yakaboylu, J. Harinck, K. G. Smit, and W. De Jong, “Supercritical water gasification of biomass: A literature and technology overview,” *Energies* **8**, 859–894 (2015).
- A. Rahbari, A. Shirazi, M. B. Venkataraman, and J. Pye, “Solar fuels from supercritical water gasification of algae: Impacts of low-cost hydrogen on reformer configurations,” *Appl. Energy* **288**, 116620 (2021).
- J. Chen, Q. Wang, Z. Xu, E. Jiaqiang, E. Leng, F. Zhang, and G. Liao, “Process in supercritical water gasification of coal: A review of fundamentals, mechanisms, catalysts and element transformation,” *Energy Convers. Manage.* **237**, 114122 (2021).
- H. Feng, J. Sun, H. Jin, J. Kou, and L. Guo, “Char suppression mechanism using recycled intermediate phenol in supercritical water gasification of coal,” *Fuel* **305**, 121441 (2021).
- D. Kim, K. K. Sakimoto, D. Hong, and P. Yang, “Artificial photosynthesis for sustainable fuel and chemical production,” *Angew. Chem. Int. Ed.* **54**, 3259–3266 (2015).
- X. Su, L. Guo, and H. Jin, “Mathematical modeling for coal gasification kinetics in supercritical water,” *Energy Fuels* **30**, 9028–9035 (2016).
- S. Balachandar and J. K. Eaton, “Turbulent dispersed multiphase flow,” *Annu. Rev. Fluid Mech.* **42**, 111–133 (2010).
- Z. Wu, G. Ou, Y. Ren, H. Jin, and L. Guo, “Particle-resolved numerical study of the forced convection heat transfer characteristics of an endothermic-biomass particle placed in supercritical water crossflow,” *Renewable Energy* **158**, 271–279 (2020).
- H. Zhang, B. Xiong, X. An, C. Ke, and J. Chen, “Numerical prediction on the drag force and heat transfer of non-spherical particles in supercritical water,” *Powder Technol.* **361**, 414–423 (2020).
- H. Jin, Y. Wang, H. Wang, Z. Wu, and X. Li, “Influence of Stefan flow on the drag coefficient and heat transfer of a spherical particle in a supercritical water cross flow,” *Phys. Fluids* **33**, 023313 (2021).
- Y. Wang, H. Wang, H. Jin, and L. Guo, “Numerical simulation of adiabatic/cooled/heated spherical particles with Stefan flow in supercritical water,” *Phys. Fluids* **33**, 053305 (2021).
- Z. Ou, L. Guo, C. Chi, J. Zhao, H. Jin, and D. Thévenin, “Fully resolved direct numerical simulation of single coal particle gasification in supercritical water,” *Fuel* **329**, 125474 (2022).
- Z. Ou, L. Guo, C. Chi, S. Zhu, C. Ren, H. Jin, and D. Thévenin, “Interface-resolved direct numerical simulations of interphase momentum, heat, and mass transfer in supercritical water gasification of coal,” *Phys. Fluids* **34**, 103319 (2022).
- S. Ganguli and S. K. Lele, “Drag of a heated sphere at low Reynolds numbers in the absence of buoyancy,” *J. Fluid Mech.* **869**, 264–291 (2019).
- R. Kurose, M. Anami, A. Fujita, and S. Komori, “Numerical simulation of flow past a heated/cooled sphere,” *J. Fluid Mech.* **692**, 332–346 (2012).
- N. Oppenheimer, S. Navardi, and H. A. Stone, “Motion of a hot particle in viscous fluids,” *Phys. Rev. Fluids* **1**, 014001 (2016).
- K. Jiang, B. Zhang, W. Wang, and H. Jin, “Effect of the variable physical properties on sub- and supercritical CO₂ flowing over a stationary spherical particle,” *Phys. Fluids* **34**, 103605 (2022).

- ²⁶T. R. Jayawickrama, N. E. L. Haugen, M. U. Babler, M. A. Chishty, and K. Umeki, "The effect of Stefan flow on the drag coefficient of spherical particles in a gas flow," *Int. J. Multiphase Flow* **117**, 130–137 (2019).
- ²⁷R. Kurose, H. Makino, S. Komori, M. Nakamura, F. Akamatsu, and M. Katsuki, "Effects of outflow from the surface of a sphere on drag, shear lift, and scalar diffusion," *Phys. Fluids* **15**, 2338–2351 (2003).
- ²⁸X. Yang, C. Duan, J. Xu, Y. Liu, and B. Cao, "A numerical study on the thermal conductivity of H₂O/CO₂/H₂ mixtures in supercritical regions of water for coal supercritical water gasification system," *Int. J. Heat Mass Transfer* **135**, 413–424 (2019).
- ²⁹C. Fan, S. Guo, and H. Jin, "Numerical study on coal gasification in supercritical water fluidized bed and exploration of complete gasification under mild temperature conditions," *Chem. Eng. Sci.* **206**, 134–145 (2019).
- ³⁰X. Yang, Y. Feng, J. Xu, J. Jin, Y. Liu, and B. Cao, "Numerical study on transport properties of the working mixtures for coal supercritical water gasification based power generation systems," *Appl. Therm. Eng.* **162**, 114228 (2019).
- ³¹S. D. Anuar Sharuddin, F. Abnisa, W. M. A. Wan Daud, and M. K. Aroua, "A review on pyrolysis of plastic wastes," *Energy Convers. Manage.* **115**, 308–326 (2016).
- ³²A. Abdelsamie, G. Fru, T. Oster, F. Dietzsch, G. Janiga, and D. Thévenin, "Towards direct numerical simulations of low-Mach number turbulent reacting and two-phase flows using immersed boundaries," *Comput. Fluids* **131**, 123–141 (2016).
- ³³C. Chi, G. Janiga, and D. Thévenin, "On-the-fly artificial neural network for chemical kinetics in direct numerical simulations of premixed combustion," *Combust. Flame* **226**, 467–477 (2021).
- ³⁴C. Chi, X. Xu, and D. Thévenin, "Efficient premixed turbulent combustion simulations using flamelet manifold neural networks: A priori and a posteriori assessment," *Combust. Flame* **245**, 112325 (2022).
- ³⁵A. Abdelsamie, S. Voß, P. Berg, C. Chi, C. Arens, D. Thévenin, and G. Janiga, "Comparing LES and URANS results with a reference DNS of the transitional airflow in a patient-specific larynx geometry during exhalation," *Comput. Fluids* **255**, 105819 (2023).
- ³⁶D. G. Goodwin, H. K. Moffat, I. Schoegl, R. L. Speth, and B. W. Weber, "Cantera: An object-oriented software toolkit for chemical kinetics, thermodynamics, and transport processes" (2022), see <https://www.cantera.org>.
- ³⁷E. Lemmon, M. Huber, and M. McLinden, "NIST standard reference database 23: Reference fluid thermodynamic and transport properties-REFPROP, version 9.1" (2013).
- ³⁸C. Chi, A. Abdelsamie, and D. Thévenin, "A directional ghost-cell immersed boundary method for incompressible flows," *J. Comput. Phys.* **404**, 109122 (2020).
- ³⁹Z. Ou, C. Chi, L. Guo, and D. Thévenin, "A directional ghost-cell immersed boundary method for low Mach number reacting flows with interphase heat and mass transfer," *J. Comput. Phys.* **468**, 111447 (2022).
- ⁴⁰Y. Lu, J. Huang, P. Zheng, and D. Jing, "Flow structure and bubble dynamics in supercritical water fluidized bed and gas fluidized bed: A comparative study," *Int. J. Multiphase Flow* **73**, 130–141 (2015).
- ⁴¹Z. Ou, H. Jin, Z. Ren, S. Zhu, M. Song, and L. Guo, "Mathematical model for coal conversion in supercritical water: Reacting multiphase flow with conjugate heat transfer," *Int. J. Hydrogen Energy* **44**, 15746–15757 (2019).
- ⁴²C. Ren, H. Jin, Z. Ren, Z. Ou, Y. Dong, Z. Cheng, and L. Guo, "Simulation of solid-fluid interaction in a supercritical water fluidized bed with a cold jet," *Powder Technol.* **363**, 687–698 (2020).
- ⁴³Z. Cheng, H. Jin, J. Chen, Z. Ren, Z. Ou, C. Ren, and L. Guo, "Numerical study on flow dynamics characteristics of supercritical water transporting particles under transcritical temperature conditions driven by pressure difference," *Powder Technol.* **363**, 676–686 (2020).
- ⁴⁴S. C. R. Dennis and G.-Z. Chang, "Numerical solutions for steady flow past a circular cylinder at Reynolds numbers up to 100," *J. Fluid Mech.* **42**, 471–489 (1970).
- ⁴⁵T. Ye, R. Mittal, H. S. Udaykumar, and W. Shyy, "An accurate Cartesian grid method for viscous incompressible flows with complex immersed boundaries," *J. Comput. Phys.* **156**, 209–240 (1999).
- ⁴⁶Y.-H. Tseng and J. H. Ferziger, "A ghost-cell immersed boundary method for flow in complex geometry," *J. Comput. Phys.* **192**, 593–623 (2003).
- ⁴⁷S. W. Churchill and M. Bernstein, "A correlating equation for forced convection from gases and liquids to a circular cylinder in crossflow," *J. Heat Transfer* **99**, 300–306 (1977).
- ⁴⁸K. V. Beard and H. R. Pruppacher, "A wind tunnel investigation of the rate of evaporation of small water drops falling at terminal velocity in air," *J. Atmos. Sci.* **28**, 1455–1464 (1971).